Belda, R.; Megías-Díaz, R.; Marco, M.; Vercher Martínez, A.; Giner Maravilla, E. (2023). Numerical analysis of the influence of triply periodic minimal surface structures morphometry on the mechanical response. Computer Methods and Programs in Biomedicine. 230. https://doi.org/10.1016/j.cmpb.2023.107342

Numerical analysis of the influence of triply periodic minimal surface structures morphometry on the mechanical response

Ricardo Belda[a,b,*], Raquel Megías[b], Miguel Marco[a], Ana Vercher-Martínez[b], Eugenio Giner[b]

[a]*Department of Mechanical Engineering, Universidad Carlos III de Madrid, Avda. de la Universidad 30, 28911, Leganés, Madrid, Spain*
[b]*Institute of Mechanical and Biomechanical Engineering - I2MB, Department of Mechanical Engineering and Materials, Universitat Politècnica de València, Camino de Vera, 46022 Valencia, Spain*

Abstract

Background and Objective: Design of bone scaffolds requires a combination of material and geometry to fulfil requirements of mechanical properties, porosity and pore size. Triply Periodic Minimal Surface (TPMS) structures have gained attention due to their similarities to cancellous bone. In this work, we aim at exploring relationships between morphometry and mechanical properties for TPMS configurations.

Methods: Eight TPMS structures are defined considering six porosity levels and their morphometry is characterized. The stiffness matrix of each structure is assessed and related to morphometry through a statistical analysis.

Results: An orthotropic mechanical behavior has been derived from the numerical homogenization. Properties decay exponentially for decreasing volume fraction. Through volume fraction variation, TPMS mechanical properties can be selected to match bone properties in a range of 0.2% to 70% of the bulk material properties.

Conclusions: The comparison between cancellous bone and TPMS morphometry, considering a unit cell size of 1.5 mm, reveals that the configurations ana-

*Corresponding author. Tel.: +34-618243486.
Email address: rbelda@ing.uc3m.es (Ricardo Belda)

lyzed in this work match the requirements of volume fraction, mean thickness and pore size. However, the TPMS studied in this work differ from cancellous bone anisotropy. The results in this paper provide a framework to select the proper TPMS configuration and its geometry for patient-specific applications.
Keywords: Triply Periodic Minimal Surface structures, homogenization, finite element method, morphometric characterization

1. Introduction

Industrial solutions require for high stiffness and strength but lightweight structures for several applications such as in aerospace, automotive or biomechanical engineering. Biomedical applications such as bone tissue scaffolds or implants require specific features to avoid stress shielding and to favor bone growth, osteointegration [1, 2, 3, 4, 5] and to permit an adequate waste and nutrient exchange with the surronding tissue [6, 7, 8]. Specifically, implants and scaffolds should have an apparent elastic modulus similar to the bone surrounding it, in combination with a porosity and pore size that bring on bone formation [3, 4]. This design methodology avoids high differences in stresses around the implant, which can induce bone density loss and fragilization and finally results in osteopenia. Several research works have been published in the last decades concerning the evaluation of materials (metals, polymers or composites) and geometries (lattices or porous) that fulfil those requirements [3, 1, 2, 4, 9], but further studies are still needed in order to develop patient-specific solutions.

The interconnected porous structure needs to mimic cancellous bone tissue to help the waste and nutrients exchange, so permeability is a major concern in scaffold design [6, 8]. Moreover, fluid flow, permeability and fluid shear stress conditions tissue proliferation and differentiation [7]. Some works in the literature have addressed this important issue, conducting computational fluid dynamic (CFD) simulations [6, 8, 7]. Fallah et al. [6] studied mass transportation and permeability and compared the results to cancellous bone and found similar

values between the scaffolds and the biological tissue. On the other hand, Fu et al. [7] evaluated permeability and fluid shear stresses through fluid-structure CFP simulations. The authors concluded that, increasing pore size increased permeability and decreased fluid shear stresses, which needs to be controlled by morphometry, because a direct cell-fluid contact should be avoided to optimize cell diferentiation [7].

Open-cell porous materials may be classified as periodic or random according to their morphology [10, 11]. These porous structures have been studied in the literature because of their enhanced mechanical characteristics mimicking nature such as cancellous bone or sponges. Among open-cell porous structures, triply periodic minimal surface (TPMS) structures have gained scientific attention for implants and bone scaffolds design, thanks to their good permeability and therefore their ease to bone growth and remodelling [12, 2]. TPMS structures are periodic geometries with a lower level of stress concentrators compared to other grid-based lattice structures [13, 14]. Level set equations determine the geometry of the TPMS [15]. This is an interesting feature, because several implicit functions may be explored to optimize the mechanical properties for the highest porosity.

Commonly, open-cell porous structures are manufactured through solid state processing (powder metallurgy, sintering of powder), liquid state processing (direct foaming) or electro-deposition [16, 17, 18]. Additive manufacturing presents excellent characteristics in comparison with the aforementioned manufacturing technologies, such as a low cost and fast prototyping. Moreover, it permits to precisely manufacture complex geometries digitally generated.

Porous biomaterials provide advantages as compared to homogeneous ones, such as mechanical properties adjustment flexibility, surface area increase and bone ingrowth stimulation thanks to pores [2]. Both large geometrical features that are comparable in size to the cellular dimensions and other that are much smaller than the cellular dimensions play important roles [1]. Tissue regenera-

tion improves in concave surfaces as compared to convex and flat surfaces and increases linearly with curvature, while a pore size in the order of few micrometers is necessary [19, 2].

Other works in the literature provide elastic properties as a function of volume fraction for some lattice and TPMS structures [16, 11, 37, 2, 38, 4]. However, some of they refer their results to a specific material [37, 2, 38, 4], contrary to our results, which are normalized by the bulk material properties.

Graded volume fraction TPMS configurations permit to adapt the scaffold to bone morphometry changes between locations [4, 5]. These structures showed a layer by layer deformation mechanism along the graded direction as opposed to shear bands for homogeneous lattices and in graded configurations loaded perpendicular to the graded direction [4, 5]. Moreover, experimental tests and numerical simulations of graded configurations found higher energy absorption of uniform configurations as compared to linearly graded [4].

Numerical homogenization of the elastic properties of lattice structures permits to characterize their macroscopic mechanical elastic response under different loading conditions, through stiffness matrix estimation. The evolution of the homogenized mechanical properties as a function of the structure volume fraction gives insight into the effect of porosity and may help to select a specific volume fraction/porosity and TPMS structure for each application. The homogenized elastic properties calculated include the morphometry influence, so they can be related through this analysis. Moreover, the equivalent mechanical constants can be used in macroscopic homogeneous numerical models in order to reduce computational cost.

In porous structures, the morphometry features influence the mechanical response [20, 21, 2]. Therefore, it is relevant to explore relationships governing mechanical response variation. Some authors have studied relationships

between morphology and the mechanical response of lattice porous structures. For example, Gibson et al. studied the mechanics of cellular materials, first in the two-dimensional case [22] and later in 3D [23]. The authors considered simplified cellular models and defined the deformation modes involved: bending, elastic buckling and plastic collapse of the struts. Analytical expressions were developed in terms of their geometrical features (strut length and thickness) and then correlated to a relative density parameter, to estimate the homogeneous mechanical response [23].

Some efforts have been made to characterize lattice structures morphometry using advanced imaging systems such as micro-computed tomography (micro-CT) or Scanning Electron Microscopy (SEM) [21, 24, 2]. Bobbert et al. [2] characterized some morphometric parameters such as volume fraction, mean thickness, pore size, surface area and anisotropy degree for four TPMS configurations. The authors highlighted that those structures, controlling porosity and pore size, showed similar mechanical, permeability and morphometric properties as compared to cancellous bone specimens, which has a major importance to enhance osseointegration. However, morpho-mechano relationships have not been provided for TPMS structures yet. Providing those expressions is relevant to select the most appropriate TPMS typology according to the application in terms of porosity, pore size, strut thickness and mechanical properties.

In this work, we aim at exploring relationships between some TPMS configurations morphometry and the subsequent mechanical constants characterizing its homogenized mechanical response. We provide the combination of morphometric parameters that control the variation in the elastic mechanical properties of TPMS structures. The results of the numerical elastic homogenization provide a framework to select the proper TPMS configuration and its geometry for each application. Furthermore, the homogenized mechanical properties obtained in this work could be used as input in finite element models at a macroscopic scale, simplifying the numerical modelling. In the present study,

2. Methods

2.1. Description of TPMS configurations

Triply periodic minimal surfaces (TPMS) can be defined as sheet or solid typologies. Sheet TPMS are composed of a single curved surface with little variation in thickness, while solid typologies are volumes created from a level set surface. TPMS structures are characterized by triply periodicity and a mean curvature of zero [15]. In order to generate the TPMS surface topologies, a cubic volume of interest is defined, where the periodic structure is generated using a level-set method. Level-set equations are a set of combined trigonometric equations that satisfy $\phi(x, y, z) = c$, where $\phi(x, y, z)$ is an iso-surface evaluated at an iso-value c [15].

To create a lattice material from the TPMS surface, two approaches may be followed: a solid network results from considering the cubic volume bounded by the minimal surface such that $\phi(x, y, z) > c$ or $\phi(x, y, z) < c$. Therefore, the level-set equation divides the volume between a solid and a void phase. In case of a sheet network, the structure is generated by offsetting the minimal surface to create a double surface by solving $-c <= \phi(x, y, z) <= c$ [15]. The double surface contains the solid phase, representing the TPMS structure. Then, a post-processing step is required to generate a solid volume from the surfaces generated.

The TPMS configurations analyzed in this work are depicted in Fig. 1. These eight configurations were generated using MSLattice software [15], and they are composed of four architectures: Gyroid (G), Schwarz Diamond (D), Fischer-Koch S (FK) and I-graph-Wrapped Package (I-WP) and each one is treated as a solid or sheet network.

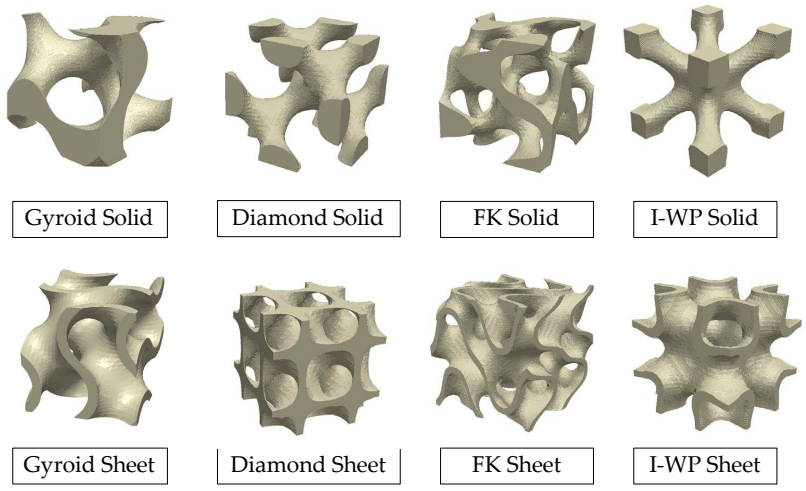

Figure 1: Representation of the eight TPMS configurations of 25 % volume fraction analyzed in this work.

The level-set equations needed to generate the TPMS architectures under study are given in Eqs. (1-4) [15]:

$$\text{Gyroid}: \ \sin X \cos Y + \sin Y \cos Z + \sin Z \cos X = c \tag{1}$$

$$\text{Schwarz Diamond}: \ \cos X \cos Y \cos Z - \sin X \sin Y \sin Z = c \tag{2}$$

$$\text{Fischer-Koch S}: \ \cos 2X \sin Y \cos Z + \cos X \cos 2Y \sin Z + \sin X \cos Y \cos 2Z = c \tag{3}$$

$$\text{I-WP}: \ 2(\cos X \cos Y + \cos Y \cos Z + \cos Z \cos X) - (\cos 2X + \cos 2Y + \cos 2Z) = c \tag{4}$$

The samples analyzed have a unit cell size of 10 mm and a cubic shape of 20 mm side. For each configuration, six levels of specimen volume fraction

(SV/TV, Structure Volume/Total Volume) are considered: 10 %, 25 %, 35 %, 50 %, 65 % and 80 %. Fig. 2 depicts the six geometries generated for FK sheet and FK solid configurations at different porosity levels.

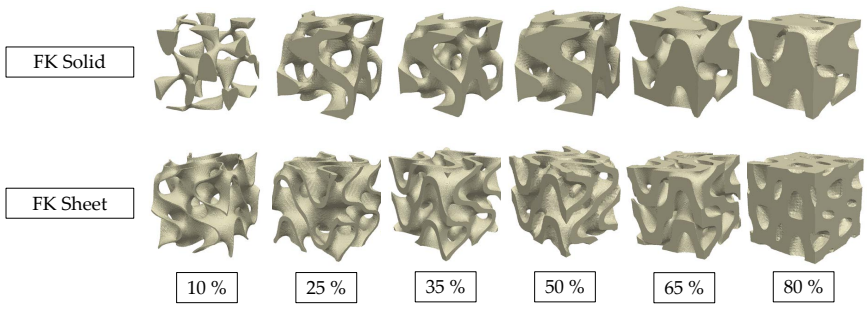

Figure 2: Representation of specimen volume fraction variation for solid and sheet Fischer-Koch TPMS configurations.

2.2. Morphometric analysis

The morphometry of each TPMS configuration is characterized by means of the following parameters, which are commonly used for porous materials characterization [20, 21]: specimen volume fraction (SV/TV), specimen external area with respect to the specimen volume (SA/SV), mean thickness (Th), mean separation (Sp), fractal dimension (D), connectivity density (Conn.D) and degree of anisotropy (DA).

We estimate all the mentioned parameters using BoneJ application [25], an open source tool for image analysis. The fractal dimension (D) is commonly used to measure the complexity of a heterogeneous structure. In this case, it is estimated through the box-counting method. Mean thickness (Th) represents the average value of the structure thickness, while mean separation (Sp) defines the mean value of the pores in the structure. Mean thickness and mean separa-

tion are calculated locally as the diameter of the greatest sphere that fits within the structure and the voids, respectively, analyzing the whole 3D digital image model (which is commonly called a mask). Therefore, a Th and Sp maps are obtained and mean values are then calculated for the whole structure[25, 28, 29]. On the other hand, the connectivity density (Conn.D) is determined by estimating the Euler number in a 3D digitized image [26]. In the case of the anisotropy degree (DA), it describes the anisotropy in material disposition (a higher DA value represents a more oriented material with respect to one specific direction, whereas a lower DA value is found for an homogeneous material) and is estimated using the mean intercept length (MIL) method [27].

2.3. Elastic properties homogenization

The homogenization of TPMS structures elastic properties is relevant to assess the influence of the architecture on the mechanical competence of a heterogeneous structure. It may help to select a TPMS configuration as a function of its geometry. These properties may be used in multiscale homogeneous models, reducing the computing needs.

The homogenization approach used in this work is preferable over standard mechanics approaches, such as uniform displacement or tractions because the procedure is independent of the number of cells used in the model. In case of those standard mechanics approaches, a number of unit cells are required to achieve the effective elastic results convergence. [30, 31, 32]

Our approach to estimate the homogenized elastic properties of an elementary representative volume (RVE) was implemented in Matlab (version R2021b) (pre- and post-processing) and Ansys (FE modeling). The Lamé-Hooke constitutive equation is given by:

$$\sigma = C\varepsilon \tag{5}$$

where $\sigma = (\sigma_{xx}\ \sigma_{yy}\ \sigma_{zz}\ \tau_{yz}\ \tau_{zx}\ \tau_{xy})^T$ is the stress vector, C is the stiffness matrix and $\varepsilon = (\varepsilon_{xx}\ \varepsilon_{yy}\ \varepsilon_{zz}\ \gamma_{yz}\ \gamma_{zx}\ \gamma_{xy})^T$ is the engineering strain vector. The stiffness matrix C of TPMS RVE is assessed through the application of six independent unitary strain fields (3 axial and 3 shear strains) in combination with periodic boundary conditions (PBC) constraints. In order to define PBC, the finite element mesh of each TPMS specimen was mirrored with respect to its three main directions, see Fig. 3 (a). This step is necessary in our approach to be able to define constraint equations between nodes at opposite faces to precisely simulate each strain case considering PBC. The finite element model after this step comprises 8 unit cells. Then, the equilibrium stress vector (σ^i) is computed for each strain field (ε^i) post processing the finite element results. Each load case, in combination with the PBC, permits to assess one of the columns of C. Fig. 3 (b) depicts the application of the 6 unitary load cases for a I-WP TPMS specimen of 10 % volume fraction.

- Load case 1: $\varepsilon^1 = (1\ 0\ 0\ 0\ 0\ 0)^T$, $C_{(:,1)} = \sigma^1$
- Load case 2: $\varepsilon^2 = (0\ 1\ 0\ 0\ 0\ 0)^T$, $C_{(:,2)} = \sigma^2$
- Load case 3: $\varepsilon^3 = (0\ 0\ 1\ 0\ 0\ 0)^T$, $C_{(:,3)} = \sigma^3$
- Load case 4: $\varepsilon^4 = (0\ 0\ 0\ 1\ 0\ 0)^T$, $C_{(:,4)} = \sigma^4$
- Load case 5: $\varepsilon^5 = (0\ 0\ 0\ 0\ 1\ 0)^T$, $C_{(:,5)} = \sigma^5$
- Load case 6: $\varepsilon^6 = (0\ 0\ 0\ 0\ 0\ 1)^T$, $C_{(:,6)} = \sigma^6$

Considering PBC on the RVE permits its response to be representative of the whole structure. Two conditions must be fulfilled, following Reisinger et al. [33]:

- The stress field must be periodic $\sigma_{ij}^+ = \sigma_{ij}^-$.
- The strain field must be periodic, so the deformed shape of opposite RVE faces must match.

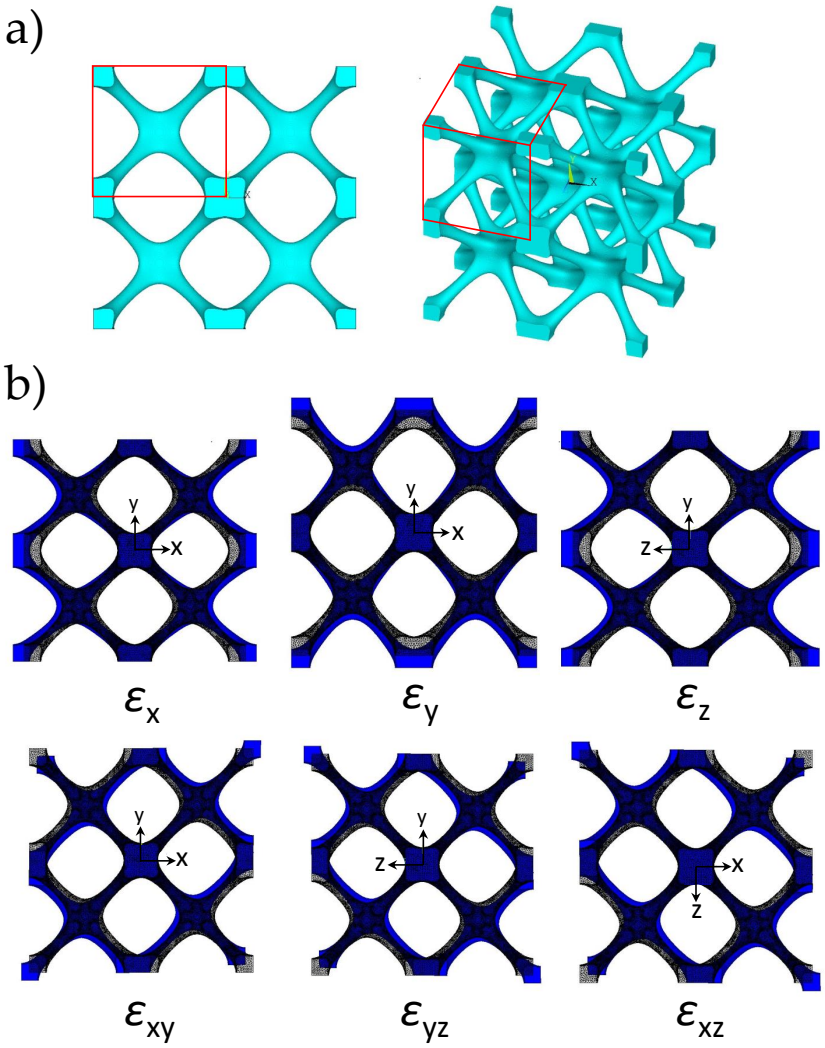

Figure 3: Representation of a) a I-WP TPMS specimen of 10 % volume fraction mesh mirroring to apply PBC (unit cell is marked within a red square) and b) the six unitary strain cases of the numerical homogenization procedure.

Therefore, constraint equations were defined on RVE faces to fulfill the PBC displacement field requirements, considering the equations proposed by Hohe [34], summarized below.

$$u^{1+} = u^{1-} + a\varepsilon_1^i \tag{6}$$

$$v^{1+} = v^{1-} + \frac{1}{2}a\varepsilon_6^i \tag{7}$$

$$w^{1+} = w^{1-} + \frac{1}{2}a\varepsilon_5^i \tag{8}$$

$$u^{2+} = u^{2-} + \frac{1}{2}b\varepsilon_6^i \tag{9}$$

$$v^{2+} = v^{2-} + b\varepsilon_2^i \tag{10}$$

$$w^{2+} = w^{2-} + \frac{1}{2}b\varepsilon_4^i \tag{11}$$

$$u^{3+} = u^{3-} + \frac{1}{2}c\varepsilon_5^i \tag{12}$$

$$v^{3+} = v^{3-} + \frac{1}{2}c\varepsilon_4^i \tag{13}$$

$$w^{3+} = w^{3-} + c\varepsilon_3^i \tag{14}$$

where a, b, c define the RVE dimensions, $^{+,-}$ define the external opposite faces at x (1), y (2) or z (3) directions and u, v and w represent displacement fields, Fig. 4. The super index i refers to the load case applied (1-6).

Using this procedure we can calculate the constitutive elastic matrix C_{ij} of the RVE, a 6x6 matrix which relates elastic stresses and strains through Hooke's law (Eq. 5). For the most general case, 36 non-zero components are needed to define the material behavior (triclinic material case). For TPMS materials with three planes of symmetry (orthotropic material case), some elements of the stiffness matrix become 0 (Eq. 15), if calculated with respect to their orientated

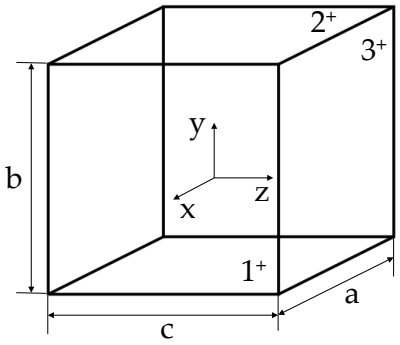

Figure 4: RVE notation scheme: a, b and c define the RVE dimensions, $N^{+,-}$ (1, 2, 3) define the opposite faces on x, y and z directions, respectively.

axes. In that case, only 9 of the 12 components are independent and can be expressed as a function of the so-called engineering constants. Those constants are the axial elastic moduli, shear elastic moduli and Poisson's ratios for the different main directions and planes: E_{x}, E_{y}, E_{z}, G_{xy}, G_{xz}, G_{yz}, ν_{xy}, ν_{xz}, ν_{yz}.

The engineering constants for an orthotropic material, such as TPMS structures, may be expressed as a function of the compliance matrix ($S_{ij} = C_{ij}^{-1}$) whose components are defined in Eq. 16. The elastic homogenization results will be presented in terms of the engineering constants in section 3.2.

$$C_{ij} = \begin{pmatrix} C_{11} & C_{12} & C_{13} & 0 & 0 & 0 \\ C_{12} & C_{22} & C_{23} & 0 & 0 & 0 \\ C_{13} & C_{23} & C_{33} & 0 & 0 & 0 \\ 0 & 0 & 0 & C_{44} & 0 & 0 \\ 0 & 0 & 0 & 0 & C_{55} & 0 \\ 0 & 0 & 0 & 0 & 0 & C_{66} \end{pmatrix} \tag{15}$$

$$S_{ij} = \begin{pmatrix} \frac{1}{E_x} & -\frac{\nu_{yx}}{E_y} & -\frac{\nu_{zx}}{E_z} & 0 & 0 & 0 \\ -\frac{\nu_{xy}}{E_x} & \frac{1}{E_y} & -\frac{\nu_{zy}}{E_z} & 0 & 0 & 0 \\ -\frac{\nu_{xz}}{E_x} & -\frac{\nu_{yz}}{E_y} & \frac{1}{E_z} & 0 & 0 & 0 \\ 0 & 0 & 0 & \frac{1}{G_{yz}} & 0 & 0 \\ 0 & 0 & 0 & 0 & \frac{1}{G_{zx}} & 0 \\ 0 & 0 & 0 & 0 & 0 & \frac{1}{G_{xy}} \end{pmatrix} \tag{16}$$

2.4. Finite element model generation

Finite element meshes of each TPMS configuration were generated using ScanIp software (Simpleware, UK). The element size was determined after a mesh sensitivity analysis, which led to the use of quadratic tetrahedral elements (SOLID92 element code in Ansys) in meshes of approximately 1M nodes and 600k elements, conducting to an element size of 0.199 mm. The mesh used for D Sheet and D Solid structures of a 25 % volume fraction is depicted in Fig. 5

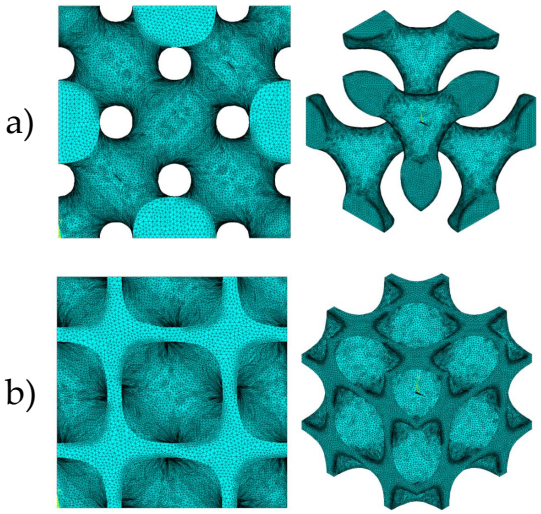

Figure 5: a) Finite element mesh used for the unit cell of D Sheet (frontal view left and isometric view right) and b) D Solid mesh (frontal view left and isometric view right) structures considering a 25 % volume fraction.

Homogeneous isotropic linear elastic material properties are considered. A Young's modulus E of 10 GPa and a Poisson's ratio ν of 0.3 were defined at the material level. In the results, we refer to material properties normalized (E_{app}/E, G_{app}/G and ν_{app}/ν) with respect to the material properties (E, G, ν). The subscript app defines the apparent mechanical properties resulting from the numerical homogenization of the elastic properties for each TPMS configuration.

2.5. Statistical analysis of morpho-mechano relationships

After representing scatter plots of morphometry vs. mechanical parameters, we evaluate relationships between them. Linear and non-linear one factor relationships are explored for each TPMS configuration. Moreover, a multi-factor statistical analysis is performed to estimate the minimum number of morphometric parameters that control the variation in TPMS mechanical properties. One- and multi-factor analyses were performed using Statgraphics Centurion 18 (version 18.1.13, Statgraphics Technologies, Inc.). We investigate the evolution of the mechanical competence of the TPMS specimens as the volume fraction (and consequently some of the morphometric parameters) is modified.

On the other hand, the Eqs. 17 and 18 are used to estimate the mechanical elastic properties as a function of the relative density (structure volume fraction in this work) for porous structures, proposed by Gibson and Ashby [23]. They depend on two parameters that can be assessed through experiments or numerical simulations and are useful to researchers to provide simple expressions to choose the most appropriate combination of porous structure and volume fraction. In this work, we also provide those constants estimated for the pooled data, i.e. considering all the TPMS data together, and for each TPMS configuration, together with the determination coefficient R^2 for each estimation, using Matlab (version R2021b).

$$\frac{E_{\text{lattice}}}{E_{\text{bulk}}} = A_1 \left(\frac{\rho_{\text{lattice}}}{\rho_{\text{bulk}}} \right)^{n_1} \tag{17}$$

$$\frac{G_{\text{lattice}}}{G_{\text{bulk}}} = A_2 \left(\frac{\rho_{\text{lattice}}}{\rho_{\text{bulk}}} \right)^{n_2} \tag{18}$$

where A_1, A_2, n_1 and n_1 are equation constants to be adjusted, while $\left(\frac{\rho_{\text{lattice}}}{\rho_{\text{bulk}}} \right)$ represents the structure volume fraction SV/TV.

3. Results

3.1. Morphometric analysis results

The results presented in this section are referred to a unit cell size of 10 mm in a sample of 20 mm side, but some of the parameters can be directly scaled for other unit cell sizes. Specifically, mean thickness Th, mean pore size Sp and fractal dimension increase linearly with decreasing unit cell size. Volume fraction and DA are constant for unit cell size variation. However, SA/SV and Conn.D increase according to a power law for a reduction in the unit cell size, so these parameters cannot be directly scaled from the results in Tables 9 to 16.

The morphometry results for each TPMS configuration are presented in Tables 9 to 16 of Appendix A. In order to analyze the variation of morphometry as a function of the structure volume fraction (SV/TV), we plot the results of Appendix A in Figures 6 to 9.

We will exclude DA and Conn.D from the statistical analysis. The reasons are that DA values are independent of the volume fraction and the TPMS configuration and their values are close to zero. DA is calculated as follows: $\text{DA} = 1 - a/b$, being a and b the ellipsoid long axis and short axis eigenvalues, respectively. Values close to zero confirm that the ellipsoid eigenvalues are very similar and there is not preference in material orientation for the TPMS configurations analyzed. In the case of cancellous bone, DA values vary according

to bone location and can take values between 0.16 and 1.18 following the same expression for DA calculation [40]. On the other hand, the connectivity density (Conn.D) is nearly constant for each TPMS configuration and independent of the volume fraction, except from few cases. In those cases, a change in volume fraction does not produce a dilatation or erosion, but a volume intersection. In two cases of 80 % volume fraction (I-WP Sheet and FK Solid), a negative Conn.D is obtained, which usually happens if there are multiple particles or enclosed cavities [25], in this case produced by a volume fraction increase. Therefore, DA and Conn.D variables are excluded for the statistical analysis to explore relationships between morphometry and the mechanical response.

3.1.1. Effect on the structure area per volume ratio SA/SV

Figure 6 depicts the variation of the structure area per volume ratio SA/SV as a function of the volume fraction SV/TV. It is observed that SA/SV decreases as SV/TV increases. Moreover, as the volume fraction increases, less differences in SA/SV are observed between TPMS configurations. This is because, as porosity decreases, structure volume increases and surface area decreases. Each TPMS configuration presents a higher SA/SV for the sheet structure typology, which were created by offsetting the TPMS. In the case of solid configurations, the SA/SV values are bonded in a narrow range independently of the volume fraction.

For applications such as bone scaffolds, it is apropriate to have a large surface area in order to permit a greater osseointegration, so it would be preferable to use sheet TPMS typologies and a low volume fraction. Specifically, FK sheet configuration presents the highest SA/SV. For 10 % volume fraction, a maximum value of 12 mm^{-1} is found, in contrast to solid type configurations, which have values around 3 mm^{-1}.

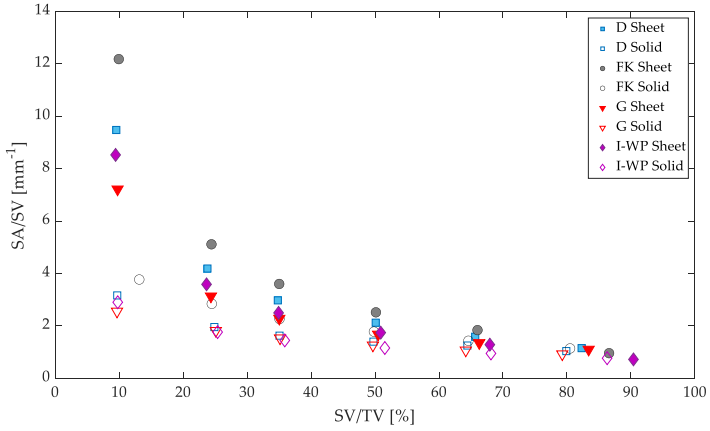

Figure 6: Area per volume ratio SA/SV as a function of volume fraction SV/TV.

3.1.2. Effect on the mean thickness Th

In Figure 7, a linear relationship is observed between the mean thickness Th and the volume fraction for all the TPMS configurations. Sheet models present less Th differences for low levels of volume fraction, which increase for higher values. For the same volume fraction, sheet configurations have lower Th values in comparison with the solid counterparts.

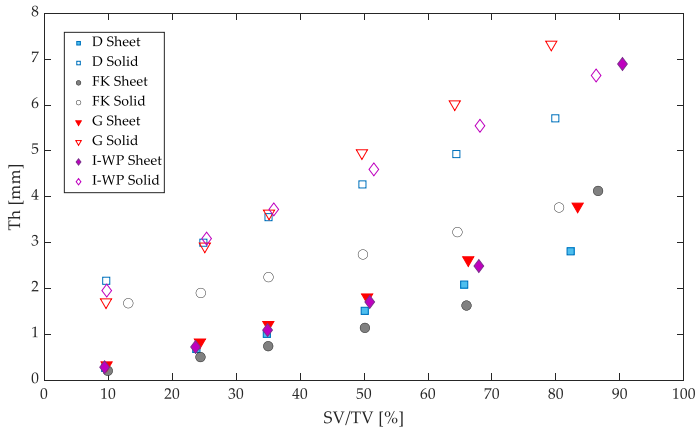

Figure 7: Mean structure thickness Th as a function of the volume fraction.

3.1.3. Effect on the mean pore size Sp

Figure 8 depicts a linear decrease of the mean pore size Sp as volume fraction increases. Solid configurations present higher Sp values in comparison with sheet configurations. For a given volume fraction, it is relevant to control pore size because, in bone scaffolds design Sp size should be similar to the pore size of the cancellous bone surrounding the scaffold, thus enhancing osteointegration [3, 9]. Pore size varies linearly with unit cell size, whose control is crucial in manufacturing (higher manufacturing errors are commonly expected for smaller cell sizes). Therefore, sheet configurations achieve pore size requirements for a larger unit cell size and would be preferred as compared to solid configurations.

On the other hand, in Figure 8, it is shown that FK sheet configuration presents the lowest mean pore size Sp. The rest of sheet configurations have a higher value that is similar between them. Regarding solid configurations, the Gyroid presents the highest Sp, with a value around 9 mm for a 10 % volume fraction.

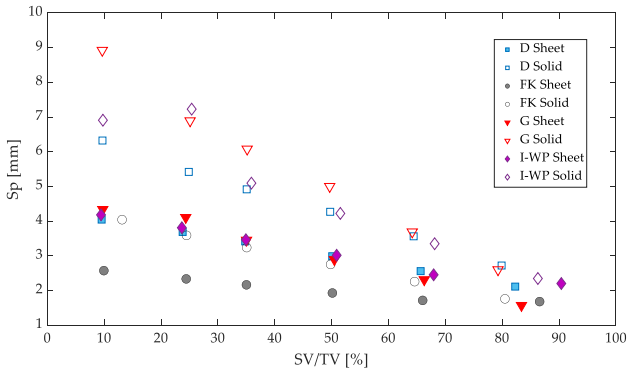

Figure 8: Mean structure separation Sp as a function of the volume fraction.

3.1.4. Effect on the fractal dimension D

The evolution of fractal dimension D as a function of the volume fraction is depicted in Figure 9. It can be observed that in solid configurations, a non-

linear relationship is found. D increases up to a 50 % of volume fraction, and then it decreases for increasing SV/TV. In general, both for sheet and solid configurations, Gyroid TPMS has the lowest D value. In sheet configurations, fractal dimension shows a decreasing trend with increasing volume fraction. A higher D value is related to a more complex surface geometry, which would enhance osseointegration, thus sheet configurations would be preferred.

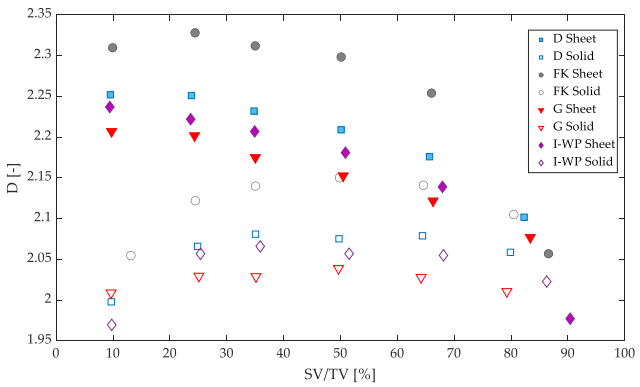

Figure 9: Representation of fractal dimension variation as a function of the volume fraction.

3.2. Estimation of the stiffness matrix results

The application of the numerical elastic homogenization procedure has permitted the estimation of the stiffness matrix C as a function of the TPMS configuration and the structure volume fraction SV/TV. The stiffness matrix estimation with respect to a coordinate system oriented along the three main directions of each structure corresponds to an orthotropic material behavior for all the TPMS configurations. Moreover, the orthotropic elastic properties are the same in the three main directions, due to the periodicity and symmetry of the TPMS structures. The zero terms of the theoretical stiffness matrix have a value ranging between $[10^{-5} - 10^{-6}]$ in our estimations, which may be neglected compared to the rest of the stiffness matrix elements. Those coefficients are related to the first and second type of mutual influence coefficients and Chentsov coefficients for a general anisotropic behavior.

As an example, Eq. 19 presents the stiffness matrix for a Diamond Sheet TPMS of 10 % volume fraction. It can be noted that minimal differences exist between directions, which may be ascribed to discretization differences in the finite element mesh at each direction and other modelling errors. These results are combined with the morphometric characterization to explore morpho-mechano relationships.

$$C_{\mathrm{D_{Sheet,10}}}[\mathrm{MPa}] = \begin{pmatrix} 266.7 & 82.0 & 82.0 & 0 & 0 & 0 \\ 82.0 & 266.3 & 81.8 & 0 & 0 & 0 \\ 82.0 & 81.8 & 266.4 & 0 & 0 & 0 \\ 0 & 0 & 0 & 38.9 & 0 & 0 \\ 0 & 0 & 0 & 0 & 39.0 & 0 \\ 0 & 0 & 0 & 0 & 0 & 39.0 \end{pmatrix} \tag{19}$$

Following Eq. 16, the elastic engineering constants can be estimated. In the case of the results in Eq. 19, an axial stiffness $E_{\mathrm{app}} = E_{\mathrm{x}} = E_{\mathrm{y}} = E_{\mathrm{z}} =$ 227.9 MPa is estimated, which corresponds to a elastic modulus E_{app}/E=0.02279, we recall that we have assumed $E = 10$ GPa. A shear elastic modulus $G_{\mathrm{app}} = G_{\mathrm{xy}} = G_{\mathrm{yz}} = G_{\mathrm{zx}} = 38.99$ MPa, corresponding to a G_{app}/G of 0.01. In case of Poisson's ratio, the numerical homogenization provides a value $\nu_{\mathrm{app}} = \nu_{\mathrm{xy}} = \nu_{\mathrm{yz}} = \nu_{\mathrm{zx}} = 0.235$ and a reduction with respect to the homogeneous material ν_{app}/ν=0.784. The stiffness matrix results for the rest of the models are presented in Appendix B and can be used in homogeneous numerical models that do not explicitly account for the structural definition, thus decreasing the computational resources needed for the simulations.

3.3. Exploring relationships between morphometry and elastic constants

In this section, we explore relationships between morphometry and elastic constants. We provide a framework for the selection of the most appropriate TPMS to match a combination of morphometry and mechanical constants. At

the end of this section, we summarize qualitatively, in Table 7, the morphometry and mechanical properties tuning possibilities of each TPMS configuration.

3.3.1. Apparent axial and shear moduli as a function of volume fraction

First, we analyze the pooled data in order to explore any general relationship for the whole set of TPMS configurations. A power law expression was found between the volume fraction and the axial and shear moduli accounting for all the configurations analyzed, see Fig. 10, in line with other results reported for lattice and porous structures [36, 23]. Values for axial and shear moduli are averaged over the 3 main directions and planes, respectively.

A non-linear increasing relationship was found between volume fraction SV/TV and the axial and shear apparent elastic moduli normalized, see Fig. 10. In general, sheet configurations present a higher axial and shear moduli as compared to their solid counterparts. This can be due to the distribution of the material through the RVE, because in solid structures the material is more concentrated and in sheet configurations material is organized as a membrane behaving more efficiently. I-WP Sheet configuration has the highest axial and shear moduli for a given volume fraction. In case of low volume fraction values (10 %), all the TPMS configurations present a very similar axial and shear apparent moduli and volume fraction drives the mechanical behavior. As volume fraction increases, the morphometry influence is higher, thus obtaining greater differences for a given volume fraction.

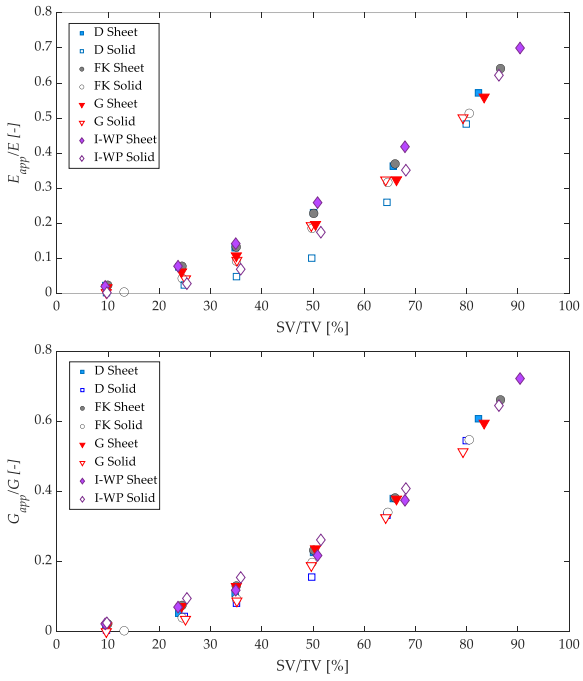

Figure 10: Representation of relationships between the axial apparent elastic modulus normalized (E_{app}/E) and the structure volume fraction (SV/TV) (top) and the shear apparent elastic modulus normalized (G_{app}/G) and the structure volume fraction (SV/TV) (bottom) for the TPMS structures analyzed.

We provide Gibson and Ashby equation parameters for the axial and shear apparent moduli (Eqs. 17 and 18) in Table 1 for both the pooled data and for each TPMS configuration, together with the coefficient of determination R^2 of each regression. These results are useful to researchers to choose the most appropriate combination of porous structure and volume fraction. Expressions for other TPMS have been reported in other works [3, 11, 38]. The results in Table 1 confirm that TPMS structures follow analogous behavior to other porous and lattice structures. The coefficient of determination increases from a 97.7 % for the pooled data to more than 99.5 % for each configuration. This coefficient is always slightly higher for solid structures. A_1 values are approximately 0.8, while the exponent n_1 is around 2 except for a value of 3 for D_{Solid}. Differences

between configurations are derived from morphometry. In the literature, A_1 is often 0.9, while n_1 is 2 for conventional foams [3], in line with our results.

Table 1: Parameters estimated for the Gibson and Ashby equations (17) and (18) for the estimation of the axial and shear moduli. The parameters correspond to an equation of the form $E_{\text{app}}/E = A_i\ (SV/TV)^{n_j}$ and $G_{\text{app}}/G = A_i\ (SV/TV)^{n_j}$, respectively. Results are provided for each TPMS and the pooled data.

	E_{app}/E			G_{app}/G		
TPMS	A_i [-]	n_j [-]	R^2[%]	A_i [-]	n_j [-]	R^2[%]
Pooled data	0.832	2.090	97.70	0.860	2.001	99.04
D_{Sheet}	0.792	1.754	99.70	0.892	1.995	99.98
D_{Solid}	0.953	3.018	99.74	0.939	2.416	99.74
FK_{Sheet}	0.821	1.813	99.68	0.853	1.848	99.78
FK_{Solid}	0.810	2.116	99.95	0.872	2.145	99.96
G_{Sheet}	0.791	2.012	99.48	0.815	1.793	99.88
G_{Solid}	0.810	2.064	99.97	0.853	2.178	99.96
$\text{I-WP}_{\text{Sheet}}$	0.825	1.702	99.93	0.873	2.027	99.49
$\text{I-WP}_{\text{Solid}}$	0.897	2.465	99.99	0.810	1.668	99.68

In the case of shear modulus normalized G_{app}/G, in Figure 10 bottom, analogous non-linear behavior is found as compared to E_{app}/E relationship. Given a 50 % porosity, shear modulus is reduced more than a 70 % from the bulk material shear modulus, reaching a 90 % reduction for 75 % - 90 % porosities (SV/TV values between 25 % - 10 %, respectively).

In Table 1, we provide the apparent shear modulus parameters for Eq. 18. A coefficient of determination $R^2 > 99\%$ has been estimated for the results, which highlights an adequate adjustment for the proven expression. The coefficient of determination is also slightly higher for solid structures, except for D solid configuration. A_2 has values close to 0.85, while n_2 takes values close to 2.

3.3.2. Apparent axial and shear moduli as a function of surface to volume ratio

Figure 11 depicts an exponential decay in E_{app}/E and G_{app}/G as the surface to volume ratio increases. Solid configuration data lay in a narrow range, while sheet configurations present a higher variation between TPMS configurations. For the unit cell dimension considered in this work (10 mm side), most of the structures analyzed have a SA/SV lower than 4 mm^{-1}. If a higher SA/SV is required, a sheet configuration would be preferable, but it implies a reduction of around 90 % in E_{app}/E.

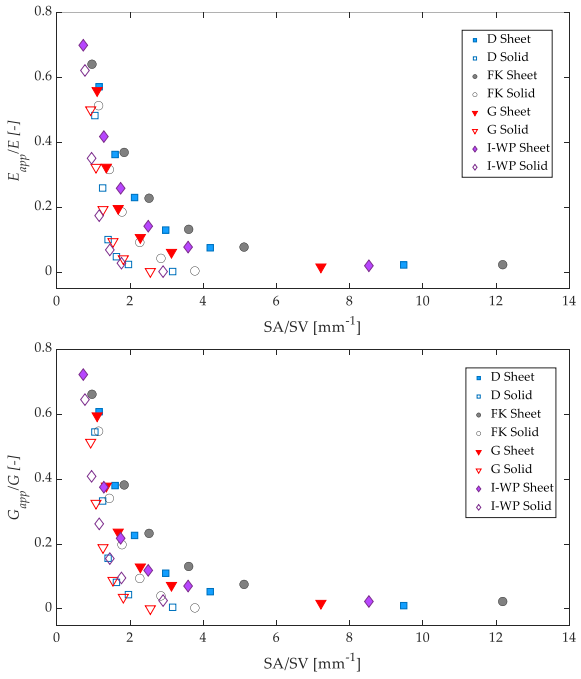

Figure 11: Representation of relationships between the axial and shear apparent elastic moduli (E_{app}/E and G_{app}/G) and the structure surface to volume ratio (SA/SV) for the TPMS structures analyzed.

For applications requiring a higher elastic modulus and SA/SV, a reduction in the unit cell size should be considered. SA/SV increases following a power law with a decreasing unit cell size, so the results presented in Figure 11 could

be scaled for other unit cell sizes.

Table 2: Parameters estimated for the axial and shear moduli as a function of the surface area to volume ratio SA/SV in the form $E_{\text{app}}/E = A_i\ e^{-n_j\ \text{SA/SV}}$ and $G_{\text{app}}/G = A_i\ e^{-n_j\ \text{SA/SV}}$. Results are provided for each TPMS and the pooled data.

	E_{app}/E			G_{app}/G		
TPMS	A_i [-]	n_j [-]	R^2[%]	A_i [-]	n_j [-]	R^2[%]
Pooled data	1.755	1.332	71.50	1.766	1.271	77.30
D_{Sheet}	1.474	0.846	98.80	1.838	0.972	99.70
D_{Solid}	21.770	3.648	98.70	12.686	3.010	98.70
FK_{Sheet}	1.141	0.609	99.40	1.193	0.620	99.50
FK_{Solid}	3.035	1.562	99.90	3.331	1.584	100.00
G_{Sheet}	3.305	1.645	97.70	2.717	1.409	98.40
G_{Solid}	6.688	2.809	100.00	7.995	2.973	100.00
$\text{I-WP}_{\text{Sheet}}$	1.339	0.906	99.60	1.573	1.092	99.20
$\text{I-WP}_{\text{Solid}}$	7.378	3.214	100.00	3.305	2.152	99.40

Table 2 shows correlations for the axial and shear moduli as a function of SA/SV ratio. No other significant relationship was found for the pooled data, which could be expected because of the notable morphological differences between configurations. On the other hand, the statistical analysis of the data obtained for each TPMS configuration led to some significant relationships between morphometry and mechanics.

3.3.3. Apparent axial and shear moduli as a function of mean thickness

Figure 12 depicts a linear relationship between the mean thickness Th and E_{app}/E and G_{app}/G. Sheet configurations present a lower Th value for the same axial or shear modulus. For low volume fractions, sheet configurations present similar Th and modulus values, while differences increase for higher Th values. Solid configurations present a wider range of Th variation, being similar to the unit cell size for high volume fraction values. Applications requiring high Th values should account for solid type configurations. The results in Figure 12

can be scaled for other unit cell sizes because Th varies linearly as a function of the unit cell size. The parameters for those linear expressions are summarized in Table 3.

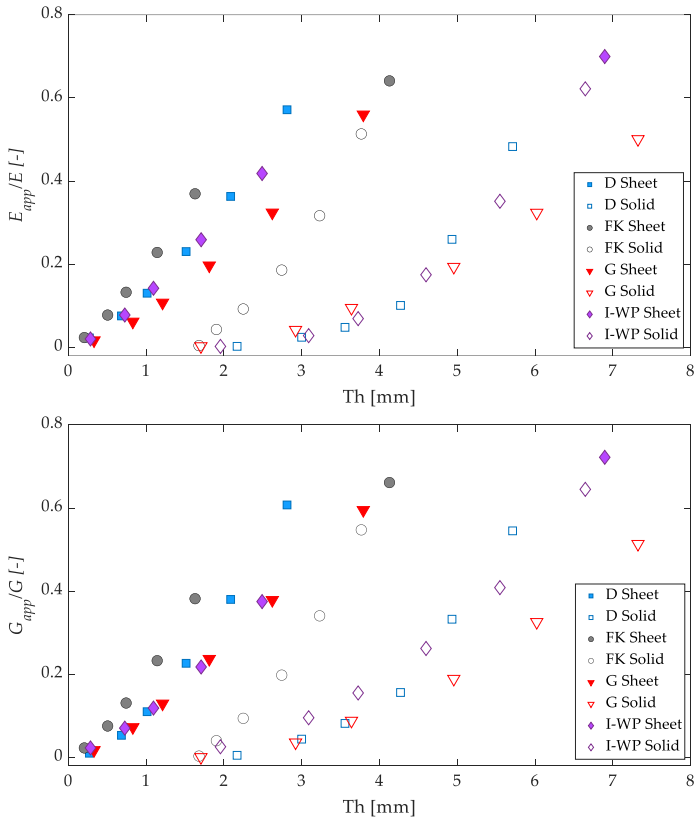

Figure 12: Representation of relationships between the axial apparent elastic modulus (E_{app}/E) and the mean structure thickness Th (top) and the shear apparent elastic modulus (G_{app}/G) and the mean structure thickness (bottom) for the TPMS structures analyzed.

Table 3: Parameters estimated for the axial and shear modulus as a function of the mean thickness Th in the form $E_{\text{app}}/E = p_i + p_j \text{Th}$ and $G_{\text{app}}/G = p_i + p_j \text{Th}$. Results are provided for each TPMS.

	E_{app}/E			G_{app}/G		
TPMS	p_i [-]	p_j [-]	R^2[%]	p_i [-]	p_j [-]	R^2[%]
D_{Sheet}	0.2167	-0.0701	98.24	0.2393	-0.1028	97.68
D_{Solid}	0.1311	-0.3634	83.34	0.1507	-0.3995	86.84
FK_{Sheet}	0.1567	0.02745	95.66	0.1626	0.0245	95.53
FK_{Solid}	0.2363	-0.4205	96.95	0.2546	-0.4568	97.10
G_{Sheet}	0.1582	-0.0682	98.49	0.17	-0.062	99.55
G_{Solid}	0.0894	-0.2029	95.26	0.09206	-0.2155	94.47
$\text{I-WP}_{\text{Sheet}}$	0.1008	0.0478	92.88	0.1057	0.02187	96.74
$\text{I-WP}_{\text{Solid}}$	0.133	-0.3586	86.24	0.1315	-0.2952	94.99

3.3.4. Apparent axial and shear moduli as a function of mean pore size

In Figure 13, it can be observed a non linear decreasing relationship between the apparent axial and shear modulus and the mean pore size Sp. The behavior depends on the TPMS. Solid configurations present higher pore sizes than sheet TPMS. Sp also varies linearly as a function of the unit cell size so the results in Figure 13 can be scaled for other unit cell sizes. Applications that require a small pore size should choose sheet typologies.The parameters for those exponential expressions are summarized in Table 13.

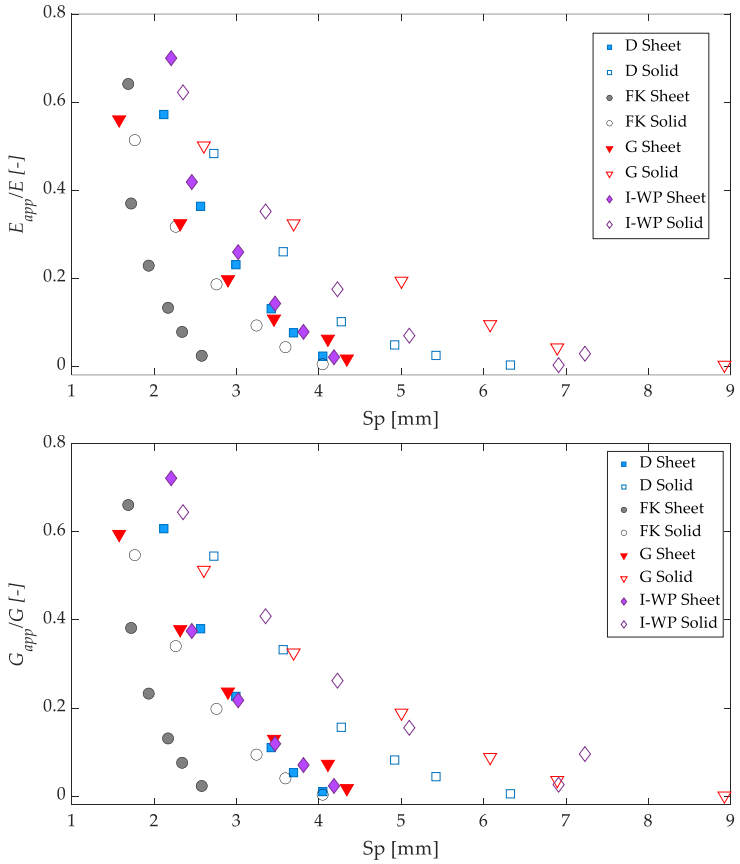

Figure 13: Representation of relationships between the axial apparent elastic modulus (E_{app}/E) and the mean structure separation Sp (top) and the shear apparent elastic modulus (G_{app}/G) and the mean structure separation (bottom) for the TPMS structures analyzed.

Table 4: Parameters estimated for the axial and shear modulus as a function of the mean pore size Sp in the form $E_{\text{app}}/E = A_i\ e^{-n_j \text{Sp}}$ and $G_{\text{app}}/G = A_i\ e^{-n_j \text{Sp}}$. Results are provided for each TPMS.

	E_{app}/E			G_{app}/G		
TPMS	A_i [-]	n_j [-]	R^2[%]	A_i [-]	n_j [-]	R^2[%]
D_{Sheet}	6.912	1.168	98.80	9.494	1.287	98.30
D_{Solid}	6.376	0.940	98.70	4.965	0.801	98.20
FK_{Sheet}	177.950	3.436	91.00	219.92	3.542	91.40
FK_{Solid}	3.981	1.149	98.70	4.355	1.162	98.40
G_{Sheet}	2.180	0.852	99.00	2.113	0.787	97.90
G_{Solid}	1.708	0.463	98.70	1.847	0.484	98.70
$\text{I-WP}_{\text{Sheet}}$	13.123	1.349	97.90	23.213	1.600	96.90
$\text{I-WP}_{\text{Solid}}$	3.152	0.683	99.10	2.088	0.496	98.70

3.3.5. Apparent axial and shear moduli as a function of fractal dimension

In case of fractal dimension D, Figure 14 shows a different relationship for sheet and solid TPMS typologies. Solid type configurations do not show correlation to the apparent axial or shear modulus. For sheet configurations E_{app}/E and G_{app}/G linearly decrease as D increases. The parameters for those linear expressions are summarized in Table 5.

Table 5: Parameters estimated for the axial and shear modulus as a function of fractal dimension D in the form $E_{\text{app}}/E = p_i + p_j \text{D}$ and $G_{\text{app}}/G = p_i + p_j \text{D}$. Solid configurations have a coefficient of determination lower than 5 %, so they are not summarized in the Table.

	E_{app}/E			G_{app}/G		
TPMS	p_i [-]	p_j [-]	R^2[%]	p_i [-]	p_j [-]	R^2[%]
D_{Sheet}	-3.542	8.038	98.38	-3.928	8.887	98.62
FK_{Sheet}	-2.095	4.98	87.87	-2.176	5.168	87.87
G_{Sheet}	-4.015	8.866	97.85	-4.318	9.547	98.77
$\text{I-WP}_{\text{Sheet}}$	-2.573	5.829	93.74	-2.689	6.064	98.23

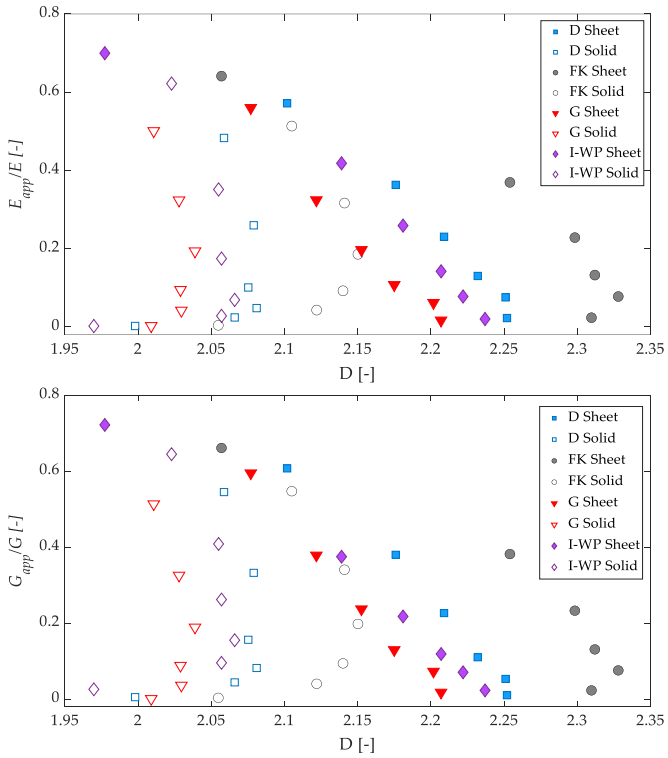

Figure 14: Representation of relationships between the axial apparent elastic modulus (E_{app}/E) and the structure fractal dimension D (top) and the shear apparent elastic modulus (G_{app}/G) and the structure fractal dimension D (bottom) for the TPMS structures analyzed.

3.3.6. Apparent Poisson's ratio as a function of morphometry

Poisson's ratio variation as a function of morphometry is depicted in Figure 15. A linear correlation can explain the relationship between morphometry and ν_{app}/ν for some TPMS, whose parameters are summarized in Table 6. Volume fraction influence, represented in Figure 15 a), shows ν_{app}/ν convergence for high SV/TV values (around 80 %). At low volume fractions, the typology has a high effect on ν_{app}/ν. For solid configurations ν_{app}/ν vary in a wider range as compared to sheet configurations. Therefore, solid TPMS configurations and low volume fractions should be selected for tuning ν_{app}/ν.

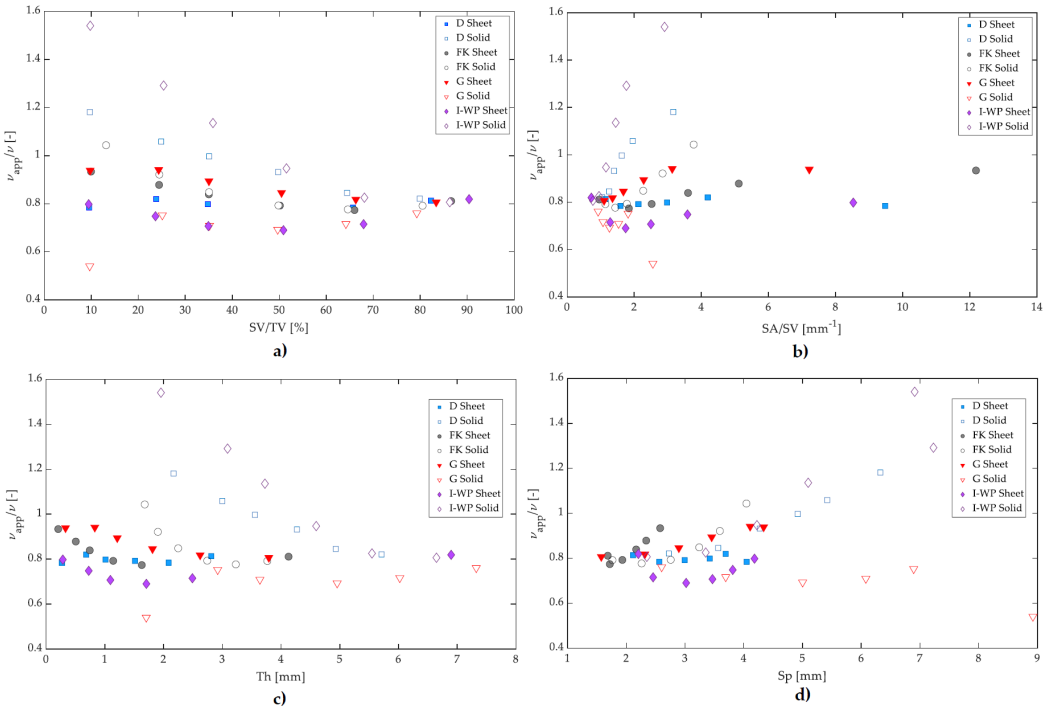

Figure 15: Representation of relationships between the apparent Poisson's ratio (ν_{app}/ν) and a) the structure volume fraction SV/TV, b) surface area to volume ratio SA/SV, c) mean thickness Th and d) mean pore size Sp for the TPMS structures analyzed.

Figure 15 b) shows that sheet TPMS structures present higher SA/SV values in combination with a low variation in the apparent Poisson's ratio ν_{app}/ν (between 0.69 and 0.94 times the bulk material Poisson's ratio). By contrast, solid TPMS structures are bounded in a smaller range of SA/SV, but are the ones with higher variation in ν_{app}/ν (between 0.54 and 1.54 times the bulk material Poisson's ratio). Therefore, these results suggest that applications requiring tuning Poisson's ratio should imply solid TPMS, while when it is needed large SA/SV values, sheet TPMS structures have to be used.

Regarding mean thickness Th, represented in Figure 15 c), the results suggest

Table 6: Parameters estimated for the apparent Poisson's ratio ν_{app}/ν as a function of morphometry in the form $\nu_{app}/\nu = p_i + p_j$ (morphometry). No significant correlations are denoted as -.

	SV/TV			SA/SV		
TPMS	p_i [-]	p_j [-]	R^2[%]	p_i [-]	p_j [-]	R^2[%]
D_{Sheet}	-	-	-	-	-	-
D_{Solid}	-0.514	1.199	96.38	0.169	0.679	90.52
FK_{Sheet}	-0.175	0.917	68.05	0.013	0.840	83.98
FK_{Solid}	-0.355	1.021	75.24	0.103	0.635	94.29
G_{Sheet}	-0.210	0.968	92.91	0.020	0.818	59.87
G_{Solid}	0.207	0.604	44.06	-0.107	0.859	63.57
$I\text{-}WP_{Sheet}$	-	-	-	-	-	-
$I\text{-}WP_{Solid}$	-0.980	1.543	91.74	0.362	0.548	94.33
	Th			Sp		
TPMS	p_i [-]	p_j [-]	R^2[%]	p_i [-]	p_j [-]	R^2[%]
D_{Sheet}	-	-	-	-	-	-
D_{Solid}	-0.103	1.379	97.13	0.103	0.505	96.76
FK_{Sheet}	-	-	-	0.157	0.513	87.24
FK_{Solid}	-0.108	1.143	70.34	0.107	0.546	77.83
G_{Sheet}	-0.044	0.951	87.48	0.054	0.705	95.00
G_{Solid}	0.025	0.583	43.18	-0.026	0.838	53.74
$I\text{-}WP_{Sheet}$	-	-	-	-	-	-
$I\text{-}WP_{Solid}$	-0.164	1.789	93.00	0.139	0.417	87.01

that sheet TPMS should be used when a low thickness in combination with ν_{app}/ν values similar to the bulk material is required. By the contrary, for aplications requiring larger values of thickness and a high prospective for tuning the apparent Poisson's ratio ν_{app}/ν, solid TPMS will be used. Finally, In case of mean pore size Sp, Figure 15 d), sheet configurations have smaller pores and bounded ν_{app}/ν values, while solid configurations present higher pore sizes and permit a higher variation in ν_{app}/ν.

Table 7: Qualitative summary of TPMS configurations morphometry and mechanical properties tuning possibilities. The following code is used: +++, ++ and + denote high, medium or low parameter tuning possibility.

	Morphometry					Mechanical properties		
TPMS	SV/TV	SA/SV	Th	Sp	D	E_{app}/E	G_{app}/G	ν_{app}/ν
D_{Sheet}	+++	+++	+	++	+++	+++	+++	++
D_{Solid}	+++	+	+++	+++	+	+++	+++	+++
FK_{Sheet}	+++	+++	+	+	+++	+++	+++	++
FK_{Solid}	+++	+	++	++	++	+++	+++	+++
G_{Sheet}	+++	++	+	++	+++	+++	+++	++
G_{Solid}	+++	+	+++	+++	+	+++	+++	+++
I-WP_{Sheet}	+++	+++	++	++	+++	+++	+++	++
I-WP_{Solid}	+++	+	+++	+++	+	+++	+++	+++

4. Discussion

In this work, we provide a detailed description of some TPMS structures morphometry as a function of volume fraction and its relationship with the elastic constants that define their mechanical behavior. The results in this work highlight TPMS structures as an interesting combination of morphometry and mechanical properties to be candidates for bone tissue scaffold design.

Bone tissue scaffold design comprises a combination of mechanical loading, geometry and substrate elastic modulus requirements [19]. As regards mechanical loading, stress shielding should be avoided, so scaffold apparent modulus needs to be similar to the one of the surrounding bone. A reduction in the apparent modulus due to porosity is beneficial. In this work, the mechanical properties provided for TPMS structures as a function of their volume fraction are normalized by the substrate material Young's modulus. Therefore, the results can be applied to any substrate elastic material. From the results presented in this work, a variation in porosity can reduce the apparent axial and

shear moduli between around a 30 % up to more than a 90 % from the bulk material properties.

Axial and shear normalized moduli provided in this work for TPMS structures are slightly lower than those obtained for lattice and porous structures in other works [16]. Although TPMS structures are a great design for implants and bone regeneration, its open-cell porous morphology leads to a elastic modulus decrease. However, their favoring to bone regeneration and absence of corners make them as one of the best options for implant designs. Presence of corners and random structures usually causes an important decrease in elastic modulus and failure load [16].

Bonatti and Mohr [35] compared a TPMS-like sheet geometry to a strut-based one (Octet-truss) and found that the former presents higher normalized Young's modulus and shear modulus for the sheet TPMS. In our results, sheet TPMS structures also presented higher elastic properties than solid structures (which are similar to strut-based geometries).

Similarly, Cao et al. [11] evaluated a novel P-lattice structure which was compared to other lattice and TPMS structures from the literature. The authors studied a narrow range of volume fraction variation (between 1 and 10 %). The axial elastic modulus of the novel P-lattice has a high similarity to the pooled data, the Gyroid sheet and solid and the solid version of FK TPMS in this work. I-WP sheet, D sheet and FK sheet present superior axial apparent properties than the ones reported by Cao et al. [11]. In adittion, other lattice structures, such as octet and honeycomb [11], have a similar axial elastic modulus than the mentioned TPMS of superior properties. Other lattice structures, such as rhombic dodecahedron and BCC, present a more flexible axial behavior as compared to the TPMS structures of this work. In case of shear properties, I-WP solid, FK sheet and G sheet present superior properties than the ones provided for the novel P-lattice in [11]. The rest of the configurations analyzed

have a similar but lower shear properties.

Other works have analyzed bioinspired sccafolds [8], to evaluated, among other, the normalized Youngâs modulus in a range of porosities between 65 % to 85 %. They aimed to mimic vertebral cancellous bone morphology and found normalized Young's modulus values very similar than the ones presented in this paper, which highlight that TPMS structures can be an optimum candidate to mimic both mechanical properties and morphometry of cancellous bone tissue.

Moreover, we provide the Gibson-Ashby parameters for the axial and shear modulus. Specifically, we estimated $A_1 = 0.832$ and $n_1 = 2.09$ and $A_2 = 0.860$ and $n_2 = 2.00$ for the pooled data for the axial and shear modulus, respectively, in the form $E_{\text{app}}/E = A_1\ (SV/TV)^{n_1}$ and $G_{\text{app}}/G = A_2\ (SV/TV)^{n_2}$. Other works report similar values for other TPMS typologies, such as $A_1 = 0.759$ and $n_1 = 1.889$ and $A_2 = 1.018$ and $n_2 = 1.98$ for a novel P-lattice structure [11] or $A_1 = 0.9$ and $n_1 = 2$ for conventional foams [3]. By contrast, Polley et al. [38] reported lower values for a sheet Gyroid ($A_1 = 0.2$ and $n_1 = 1.2$), which may be explained because the inherent defects of additive manufacturing.

On the other hand, morphometry plays an important role in osseointegration. Porosity, pore size, surface area to volume ratio and strut thickness have a major importance in order to stimulate bone formation. Our morphometry results are referred to a unit cell size of 10 mm but, as mentioned above, the results of pore size and thickness can be scaled to other unit cell sizes. In case of volume fraction and anisotropy degree, the values are constant for a unit cell size variation, while, in case of SA/SV and Conn.D, a non-linear relationship controls the influence of the unit cell size.

In the literature, pore size is recommended to be between 200-600 μm in order to increase implant cell seeding efficiency and to induce bone tissue vascularization [9, 39, 3]. This condition would be achieved with our designs for a

unit cell size of 1.5 mm side, which is commonly used as scaffold unit cell size, and for most of the volume fraction values evaluated.

Table 8: Morphometry comparison of human cancellous bone from different locations, TPMS structures from the literature and the TPMS structures analyzed in this work. We have scaled to unit cell size of 1.5 mm the morphometry results of this work to make them comparable to other results in the literature.

Morphometry	TPMS [Current work]	TPMS [2]	Lattice Cubic/Diamond [37]	Femoral head [40]	Iliac crest [40]	Lumbar spine [40]	Femoral neck [41]	Greater trochanter [41]	Vertebrae [41]
SV/TV [%]	9.44-90.4	29-61	11-36	8-32	6-28	4-12	25±6	10±2	11±3
Th [μm]	30.8-1098.6	244-444	240-823	120-257	101-225	82-157	178±27	133±14	141±17
Sp [μm]	236.1-1338.5	361-896	641-1452	480-984	523-1306	612-1269	620±82	966±146	922±151
DA [-]	0.0036-0.026	0.13-0.36	-	1.27-2.18	1.17-1.97	1.16-1.96	-	-	-

Several works in the literature report some morphometry values for human trabecular bone from different locations [40, 41]. We summarize those data together with our morphometry results and TPMS results from the literature in Table 8. First, the morphometric characterization conducted in this work covers a wider range of parameter variation as compared to other TPMS or lattice structures evaluated in the literature. For example, we study a range of SV/TV between 9.44 and 90.4 %, which consequently implies a wider range of variation in the rest of morphometric parameters. Nevertheless, the mean thickness Th, the mean pore size Sp are in the same range than cubic and diamond lattice and sheet TPMS structures [37, 2]. In case of anisotropy degree DA, our results point out to a more isotropic mechanical behavior in comparison with the results reported by Bobbert et al. [2].

Scaffolds morphometry should be similar to the one of cancellous bone in the vicinity [3, 4]. This is accomplished in the TPMS evaluated in this work except from the anisotropy degree, see Table 8. Cancellous bone usually presents material anisotropy as a function of the loads magnitude and direction applied. In the literature, cancellous bone DA values can be found between 1.16 and 2.18

[40, 41]. In order to compare those values with the ones provided in this work and the ones reported by Bobbert et al. [2] it is necessary to take into account the calculation expression used by the authors. In the case of the values provided in this work for TPMS structures the expression used is: DA $= 1 - a/b$, being a and b the ellipsoid long axis and short axis eigenvalues, respectively. In the case of the values provided for cancellous bone the expression used is: DA $= a/b$. Therefore, comparable TPMS DA values in Table 8 would be in the range 1.0036-1.026 for this work and 1.13-1.36 for the results from Bobbert et al. [2].

This work has some limitations that need to be mentioned. First, it focuses on the apparent elastic properties of TPMS structures and their relationship with morphometry. Failure is not accounted in this work because it is hypothesized that bone failure would occur prior to scaffold failure and the elastic properties control the stress shielding effect. Moreover, the numerical study evaluates ideal geometries. The effective elastic properties of triply periodic structures have theoretically the same value for C_{11}, C_{22} and C_{33}. However, in our results, slight differences (lower than 0.1 %) were obtained, which resulted from mesh differences between the corresponding RVE faces. Scaffolds permeability is known to have a major importance on their performance and it is not directly accounted in this manuscript. This issue should be solved in future works to evaluate the best combination of morphometry that optimizes bone scaffold permeability. As regards morphometry, we have characterized a unit cell of 10 mm side. We have claimed that most of the parameters calculated can be directly used or scaled for other unit cell sizes. In case of surface to volume ratio SA/SV and connectivity density Conn.D, whose calculation for other unit cell sizes would be necessary due to their non-linear relationship to the cell size.

5. Conclusions

In this work, we evaluate relationships between morphometry and elastic mechanical properties for 8 TPMS configurations to be used in biomedical applications such as bone scaffolds and implants design. The expressions reported permit the selection of the most appropriate combination of TPMS configuration and volume fraction for the requirements of the application. Thus, scaffold design can be tuned accordingly to the bone characteristics in the vicinity, avoiding stress shielding and stimulating osseointegration.

As regards morphometry, we characterized each configuration as a function of the volume fraction. Sheet configurations present a higher surface area to volume ratio SA/SV as compared to their solid counterparts and permit design flexibility to match SA/SV requirements. In addition, solid configurations permit more pore size tuning than sheet configurations. Cancellous bone and TPMS-based scaffold morphometry comparison, considering a unit cell size of 1.5 mm, reveals that the configurations studies in this work match the requirements of volume fraction, mean thickness and pore size. However, the TPMS structures of this work differ from the anisotropy found in cancellous bone tissue.

Moreover, we have calculated the stiffness matrix of each TPMS configuration as a function of its porosity. An orthotropic material behavior has been derived from the numerical simulations. Our results confirm an exponential reduction of the orthotropic mechanical properties for increasing values of porosity (i.e. decreasing volume fraction). TPMS apparent axial and shear mechanical properties can be chosen to match cancellous bone ones in a range between 0.2 % and 70 % of the bulk material properties. Solid configurations permit a higher variation in Poisson's ratio values. In addition, sheet configurations have superior axial properties than solid configurations, but in case of shear properties, I-WP solid presents the highest values as a function of porosity.

Significant relationships are provided between morphometry and mechanical properties. The TPMS configurations evaluated follow the Gibson-Ashby equation parameters, which are provided in this work for the apparent axial and shear moduli as a function of the volume fraction for both the pooled data and each configuration. A_i constant has a value close to 0.8, while exponent n is close to 2 for both axial and shear properties of the pooled data. A exponential reduction was found in E_{app}/E and G_{app}/G as the surface to volume ratio increases. On the other hand, a linear expression was found for each TPMS as a function of the mean thickness, while pore size Sp affects as an exponential decay function to the mechanical properties. In case of fractal dimension, a linear relationship explains the axial and shear properties variation for sheet configurations. In case of Poisson's ratio, the parameters evaluated do not explain the results variation for the pooled data. Solid TPMS and FK sheet and G sheet configurations show a linear correlation to morphometry (SV/TV, SA/SV, Th and Sp).

The expressions provided for the apparent mechanical properties and scaffold morphometry enable the selection of the most appropriate TPMS configuration, porosity and pore size according to the requirements of the application. Thus, they permit to define patient-specific solutions that optimize osteointegration avoiding elastic modulus impairments.

Declaration of competing interest

The authors declare no competing interests.

Acknowledgments

This work was supported by the Spanish Ministerio de Ciencia e Innovación MCIN/AEI/10.13039/501100011033 through grant numbers PID2020-118480RB-C21, PID2020-118920RB-I00 and PID2020-112628RA-I00, the European Union NextGenerationEU/PRTR through grant number PDC2021-121368-

C22 and the Generalitat Valenciana (Programme PROMETEO 2021/046 and Plan FDGENT 2018 GVA).

References

[1] Chen H, Han Q, Wang C, Liu Y, Chen B, Wang J. Porous scaffold design for additive manufacturing in orthopedics: a review. Front. Bioeng. Biotechnol. 2020;8:609. https://doi.org/10.3389/fbioe.2020.00609

[2] Bobbert FSL, Lietaert K, Eftekhari AA, Pouran B, Ahnmadi SM, Weinans H, Zadpoor AA. Additively manufactured metallic porous biomaterials based on minimal surfaces: a unique combination of topological, mechanical, and mass transport properties. Acta Biomaterialia 2017;53:572-84. https://doi.org/10.1016/j.actbio.2017.02.024

[3] Murr LE. Open-cellular metal implant design and fabrication for biomechanical compatibility with bone using electron beam melting. J. Mech. Behav, Biomed. Mat. 2017;76:164-77 dx.doi.org/10.1016/j.jmbbm.2017.02.019

[4] Afshar M, Pourkamali Anaraki A, Montazerian H, Kadkhodapour J. Additive manufacturing and mechanical characterization of graded porosity scaffolds designed based on triply periodic minimal surface architectures. J. Mech. Behav. Biomed. Mat. 2016;62:481-94. https://doi.org/10.1016/j.jmbbm.2016.05.027

[5] Al-Ketan O, Lee DW, Rowshan R, Al-Rub RKA. Functionally graded and multi-morphology sheet TPMS lattices: design, manufacturing, and mechanical properties. J. Mech. Behav. Biomed. Mat. 2020;102:103520. https://doi.org/10.1016/j.jmbbm.2019.103520

[6] Fallah A, Altunbek M, Bartolo P, Cooper G, Weightman A, Blunn G, Koc B. 3D printed scaffold design for bone defects with improved mechanical and biological properties. J. Mech. Behav. Biomed. Mater. 2022;105418. https://doi.org/10.1016/j.jmbbm.2022.105418

[7] Fu M, Wang F, Lin G. Design and research of bone repair scaffold based on two-way fluid-structure interaction. Comput. Methods Programs Biomed. 2021;204:106055. https://doi.org/10.1016/j.cmpb.2021.106055

[8] Li X, Wang Y, Zhang B, Yang H, Mushtaq RT, Liu M, Bao C, Shi Y, Luo Z, Zhang W. The design and evaluation of bionic porous bone scaffolds in fluid flow characteristics and mechanical properties. Comput. Methods Programs Biomed. 2022;225:107059. https://doi.org/10.1016/j.cmpb.2022.107059

[9] Karageorgiou V, Kaplan D. Porosity of 3D biomaterial scaffolds and osteogenesis. Biomaterials 2005;26:5474-91. doi:10.1016/j.biomaterials.2005.02.002

[10] Wang Y, Zhang L, Daynes S, Zhang H, Feih S, Wang MY. Design of graded lattice structure with optimized mesostructures for additive manufacturing. Mater. Des. 2018;142:114-23. https://doi.org/10.1016/J.MATDES.2018.01.011.

[11] Cao X, Zhang D, Liao B, Fang S, Liu L, Gao R, Li Y. Numerical analysis of the mechanical behavior and energy absorption of a novel P-lattice. Thin-Walled Struct. 2020;157:107147. https://doi.org/10.1016/j.tws.2020.107147

[12] Olivares AL, Marsal E, Planell JA, Lacroix D. Finite element study of scaffold architecture design and culture conditions for tissue engineering. Biomaterials 2009;30(30):6142–49. doi:10.1016/j.biomaterials.2009.07.041

[13] Yánez A, Cuadrado A, Martel O, Alfonso H, Monopoli D. Gyroid porous titanium structures: A versatile solution to be used as scaffolds in bone defect reconstruction. Mater. Des. 2018;140:21–29 doi:10.1016/j.matdes.2017.11.050

[14] Zhong M, Zhou W, Xi H, Liang Y, Wu Z. Double-level energy absorption of 3D printed TPMS cellular structures via wall thickness gradient design. Materials 2021;14(21):6262 doi:10.3390/ma14216262

[15] Al-Ketan O, Al-Rub RKA. MSLattice: A free software for generating uniform and graded lattices based on triply periodic minimal surfaces. Mat. Design Process Comm. 2020;e205. https://doi.org/10.1002/mdp2.205

[16] Marco M, Belda R, Miguélez MH, Giner E. Numerical analysis of mechanical behaviour of lattice and porous structures. Compos. Struct. 2021;261:113292. https://doi.org/10.1016/j.compstruct.2020.113292

[17] Ryan G, Pandit A, Apatsidis D. Fabrication methods of porous metals for use in orthopaedic applications. Biomaterials 2006;27(13):2651-70. https://doi.org/10.1016/j.biomaterials.2005.12.002.

[18] Banhart J. Manufacture, characterisation and application of cellular metals and metal foams. Prog. Mater. Sci. 2001;46(6):559-632. https://doi.org/10.1016/S0079-6425(00)00002-5.

[19] Zadpoor AA. Bone tissue regeneration: the role of scaffold geometry. Biomater. Sci. 2015;3:231-45. https://doi.org/10.1039/c4bm00291a

[20] Belda R, Palomar M, Peris-Serra JL, Vercher-Martínez A, Giner E. Compression failure characterization of cancellous bone combining experimental testing, digital image correlation and finite element modeling. Int. J. Mech. Sci. 2020;165:105213. https://doi.org/10.1016/j.ijmecsci.2019.1052

[21] Belda R, Palomar M, Marco M, Vercher-Martínez A, Giner E. Open cell polyurethane foam compression failure characterization and its relationship to morphometry. Mater. Sci. Eng. C. 2021;120:111754. https://doi.org/10.1016/j.msec.2020.111754

[22] Gibson LJ, Ashby MF, Schajer GS, Robertson CI. The mechanics of two-dimensional cellular materials. Proc. R Soc A Math. Phys. Eng. Sci. 1982;382:25–42. doi:10.1098/rspa.1982.0087

[23] Gibson LJ, Ashby MF. The mechanics of three-dimensional cellular materials. Proc. R Soc. A Math. Phys. Eng. Sci. 1982;382:43–59. doi:10.1098/rspa.1982.0088

[24] Gómez S, Vlad MD, López J, Navarro M, Fernández E. Characterization and three-dimensional reconstruction of synthetic bone model foams. Mater. Sci. Eng. C 2013;33(6):3329–35. doi:10.1016/j.msec.2013.04.013

[25] Doube M, Klosowski MM, Arganda-Carreras I, Cordelières FP, Dougherty RP, Jackson JS, Schmid B, Hutchinson JR, Shefelbine SJ. BoneJ: Free and extensible bone image analysis in ImageJ. Bone 2010;47:1076–79. doi:10.1016/j.bone.2010.08.023

[26] Toriwaki J, Yonekura T. Euler number and connectivity indexes of a three dimensional digital picture. Forma 2002;17:183–209.

[27] Harrigan TP, Mann RW. Characterization of microstructural anisotropy in orthotropic materials using a second rank tensor. J Mater Sci 1984;19:761–7. https://doi.org/10.1007/BF00540446

[28] Hildebrand t, Rüegsegger P. A new method for the model-independent assessment of thickness in three-dimensional images. J. Microsc. 1997;185: 67-75. https://doi.org/10.1046/j.1365-2818.1997.1340694.x

[29] Dougherty R, Kunzelmann K. Computing local thickness of 3D structures with ImageJ. Microsc. Microanal. 2007;13: 1678-1679. https://doi.org/10.1017/S1431927607074430

[30] Hollister SJ, Kikuchi N. A comparison of homogenization and standard mechanics analyses for periodic porous composites. Comput. Mech. 1992;10:73-95. https://doi.org/10.1007/BF00369853

[31] Coelho PG, Hollister SJ, Flanagan CL Fernandes PR. Bioresorbable scaffolds for bone tissue engineering: Optimal design, fabrication, mechanical testing and scale-size effects analysis. Med. Eng. Phys. 2015;287-96. https://doi.org/10.1016/j.medengphy.2015.01.004

[32] Pecullan S, Gibiansky LV, Torquato S. Scale effects on the elastic behavior of periodic and hierarchical two-dimensional composites. J. Mech. Phys. Solids 1999;47:1509-42.

[33] Reisinger AG, Pahr DH, Zysset PK. Elastic anisotropy of bone lamellae as a function of fibril orientation pattern. Biomech. Model Mechanobiol. 2011;10:67–77. https://doi.org/10.1007/s10237-010-0218-6

[34] Hohe J. A direct homogenization approach for determination of the stiffness matrix for microheterogeneous plates with application to sandwich panels. Compos. Part B- Eng. 2003;34:615–626. https://doi.org/10.1016/S1359-8368(03)00063-5

[35] Bonatti C, Mohr D. Mechanical performance of additively-manufactured anisotropic and isotropic smooth shell-lattice materials: Simulations and experiments. J. Mech. Phys. Solids 2019;122:1-26. https://doi.org/10.1016/j.jmps.2018.08.022

[36] Keaveny TM, Morgan EF, Niebur GL, Yeh OC. Biomechanics of trabecular bone. Annu. Rev. Biomed. Eng. 2001;3:307–33. https://doi.org/10.1146/annurev.bioeng.3.1.307

[37] Kadkhodapour J, Montazerian H, Darabi ACh, Anaraki AP, Ahmadi SM, Zadpoor AA, Schmauder S. Failure mechanisms of additively manufactured porous biomaterials: Effects of porosity and type of unit cell. J. Mech. Behav. Biomed. Mat. 2015;50:180-91. https://doi.org/10.1016/j.jmbbm.2015.06.012

[38] Polley C, Radlof W, Hauschulz F, Benz C, Sander M, Seitz H. Morphological and mechanical characterisation of three-dimensional gyroid structures fabricated by electron beam melting for the use as porous biomaterials. J. Mech. Behav. Biomed. Mat. 2022;125:104882. https://doi.org/10.1016/j.jmbbm.2021.104882

[39] Senatov FS, Niaza KV, Stepashkin AA, Kaloshin SD. Low-cycle fatigue behavior of 3d-printed PLA-based porous scaffolds. Compos. B. Eng 2016;97:193–200 doi:10.1016/j.compositesb.2016.04.067

[40] Ulrich D, van Rietbergen B, Laib A, Ruegsegger P. The ability of three-dimensional structural indices to reflect mechanical aspects of trabecular bone. Bone 1999;25:55-60. https://doi.org/10.1016/S8756-3282(99)00098-8

[41] Bevill G, Keaveny TM. Trabecular bone strength predictions using finite element analysis of micro-scale images at limited spatial resolution. Bone 2009;44:579-584. https://doi.org/10.1016/j.bone.2008.11.020

Appendix A: Morphometry results of TPMS structures.

Table 9: Morphometric parameters of D_{Sheet} configuration.

	D_{Sheet}					
Ideal SV/TV [%]	10	25	35	50	65	80
Actual measured SV/TV [%]	9.55	23.80	34.80	50.10	65.66	82.29
SA/SV [mm^{-1}]	9.48	4.19	2.98	2.12	1.59	1.15
Th [mm]	0.27	0.68	1.01	1.51	2.09	2.81
Sp [mm]	4.05	3.69	3.42	2.99	2.56	2.12
D [-]	2.252	2.251	2.232	2.209	2.176	2.102
Conn.D [mm^{-3}]	0.017	0.017	0.017	0.017	0.017	0.017
DA [-]	0.010	0.0081	0.009	0.010	0.011	0.018

Table 10: Morphometric parameters of D_{Solid} configuration.

	D_{Solid}					
Ideal SV/TV [%]	10	25	35	50	65	80
Actual measured SV/TV [%]	9.70	24.88	35.07	49.75	64.43	79.90
SA/SV [mm^{-1}]	3.17	1.96	1.63	1.40	1.25	1.04
Th [mm]	2.17	3.00	3.56	4.27	4.93	5.71
Sp [mm]	6.33	5.42	4.92	4.27	3.57	2.72
D [-]	1.998	2.066	2.081	2.075	2.079	2.059
Conn.D [mm^{-3}]	0.009	0.009	0.009	0.003	0.009	0.009
DA [-]	0.009	0.005	0.017	0.019	0.017	0.015

Table 11: Morphometric parameters of G_{Sheet} configuration.

	G_{Sheet}					
Ideal SV/TV [%]	10	25	35	50	65	80
Actual measured SV/TV [%]	9.75	24.34	35.04	50.48	66.29	83.39
SA/SV [mm^{-1}]	7.22	3.13	2.28	1.68	1.35	1.10
Th [mm]	0.33	0.83	1.21	1.81	2.62	3.79
Sp [mm]	4.34	4.11	3.45	2.90	2.32	1.57
D [-]	2.207	2.202	2.175	2.153	2.122	2.077
Conn.D [mm^{-3}]	0.009	0.009	0.009	0.009	0.003	0.009
DA [-]	0.010	0.010	0.008	0.009	0.011	0.018

Table 12: Morphometric parameters of G_{Solid} configuration.

	G_{Solid}					
Ideal SV/TV [%]	10	25	35	50	65	80
Actual measured SV/TV [%]	9.66	25.11	35.15	49.67	64.18	79.27
SA/SV [mm^{-1}]	2.56	1.82	1.53	1.26	1.07	0.93
Th [mm]	1.70	2.92	3.64	4.96	6.02	7.32
Sp [mm]	8.92	6.89	6.08	5.00	3.69	2.60
D [-]	2.009	2.030	2.029	2.039	2.028	2.011
Conn.D [mm^{-3}]	0.005	0.005	0.005	0.005	0.005	0.005
DA [-]	0.015	0.006	0.021	0.013	0.011	0.015

Table 13: Morphometric parameters of FK_{Sheet} configuration.

	FK_{Sheet}					
Ideal SV/TV [%]	10	25	35	50	65	80
Actual measured SV/TV [%]	9.94	24.43	35.02	50.13	66.02	86.59
SA/SV [mm^{-1}]	12.18	5.12	3.60	2.52	1.84	0.96
Th [mm]	0.21	0.51	0.74	1.14	1.63	4.13
Sp [mm]	2.58	2.34	2.17	1.93	1.72	1.68
D [-]	2.310	2.328	2.312	2.298	2.254	2.057
Conn.D [mm^{-3}]	0.041	0.041	0.041	0.041	0.031	-0.017
DA [-]	0.010	0.0120	0.011	0.011	0.008	0.026

Table 14: Morphometric parameters of FK_{Solid} configuration.

	FK_{Solid}					
Ideal SV/TV [%]	10	25	35	50	65	80
Actual measured SV/TV [%]	13.14	24.48	35.06	49.82	64.60	80.49
SA/SV [mm^{-1}]	3.77	2.84	2.27	1.78	1.43	1.14
Th [mm]	1.68	1.90	2.25	2.74	3.23	3.77
Sp [mm]	4.04	3.59	3.24	2.76	2.26	1.76
D [-]	2.055	2.122	2.140	2.150	2.141	2.105
Conn.D [mm^{-3}]	0.021	0.021	0.021	0.021	0.021	0.021
DA [-]	0.010	0.013	0.013	0.004	0.019	0.015

Table 15: Morphometric parameters of I-WP$_{\text{Sheet}}$ configuration.

	I-WP$_{\text{Sheet}}$					
Ideal SV/TV [%]	10	25	35	50	65	80
Actual measured SV/TV [%]	9.44	23.66	34.92	50.89	67.95	90.40
SA/SV [mm^{-1}]	8.53	3.59	2.50	1.74	1.29	0.72
Th [mm]	0.28	0.73	1.09	1.71	2.49	6.90
Sp [mm]	4.18	3.81	3.47	3.02	2.46	2.21
D [-]	2.24	2.22	2.21	2.18	2.14	1.98
Conn.D [mm^{-3}]	0.013	0.013	0.013	0.013	0.013	-0.005
DA [-]	0.007	0.007	0.012	0.018	0.012	0.009

Table 16: Morphometric parameters of I-WP$_{\text{Solid}}$ configuration.

	I-WP$_{\text{Solid}}$					
Ideal SV/TV [%]	10	25	35	50	65	80
Actual measured SV/TV [%]	9.77	25.39	35.89	51.53	68.12	86.28
SA/SV [mm^{-1}]	2.90	1.77	1.45	1.16	0.95	0.77
Th [mm]	1.96	3.09	3.73	4.60	5.55	6.65
Sp [mm]	6.91	7.23	5.10	4.22	3.35	2.35
D [-]	1.970	2.057	2.066	2.057	2.055	2.023
Conn.D [mm^{-3}]	0.007	0.007	0.007	0.007	0.007	0.007
DA [-]	0.008	0.0087	0.012	0.006	0.012	0.011

Appendix B: Stiffness matrix of TPMS structures as a function of the volume fraction.

In the following, we provide the non-zero components of the stiffness matrix C according to Eq. 15.

Table 17: Non-zero components of the stiffness matrix C [MPa] of D_{Sheet} configuration as a function of the volume fraction.

	D_{Sheet}								
SV/TV [%]	C_{11}	C_{12}	C_{13}	C_{22}	C_{23}	C_{33}	C_{44}	C_{55}	C_{66}
10	266.7	82.0	82.0	266.3	81.8	266.4	38.9	39.0	39.0
25	903.6	294.4	294.2	901.8	294.4	901.9	204.4	204.5	204.6
35	1536.4	483.6	483.5	1534.9	483.1	1534.5	423.2	423.4	423.5
50	2710.3	843.7	843.7	2704.4	842.5	2704.7	870.4	870.8	871.5
65	4252.7	1306.4	1307.2	4240.7	1304.8	4245.0	1461.0	1462.1	1462.1
80	6798.5	2190.9	2192.1	6777.4	2186.8	6781.1	2334.5	2337.2	2336.6

Table 18: Non-zero components of the stiffness matrix C [MPa] of D_{Solid} configuration as a function of the volume fraction.

	D_{Solid}								
SV/TV [%]	C_{11}	C_{12}	C_{13}	C_{22}	C_{23}	C_{33}	C_{44}	C_{55}	C_{66}
10	41.5	22.7	22.8	41.4	22.7	41.4	19.5	19.5	19.5
25	346.5	161.2	161.3	346.2	161.1	346.1	169.2	169.4	169.3
35	647.9	276.7	276.4	647.7	276.1	647.4	314.5	314.8	315.0
50	1291.0	500.5	501.1	1288.6	499.8	1289.0	600.2	601.3	600.8
65	3146.2	1068.3	1069.0	3136.9	1064.4	3138.9	1276.5	1280.2	1279.7
80	5766.7	1882.8	1881.8	5752.8	1879.5	5753.3	2095.2	2096.6	2097.5

Table 19: Non-zero components of the stiffness matrix C [MPa] of FK_{Sheet} configuration as a function of the volume fraction.

	FK_{Sheet}								
SV/TV [%]	C_{11}	C_{12}	C_{13}	C_{22}	C_{23}	C_{33}	C_{44}	C_{55}	C_{66}
10	302.9	117.9	117.8	302.6	117.8	302.7	87.9	88.0	88.0
25	959.8	343.5	343.4	959.7	343.1	958.7	290.8	290.7	291.0
35	1597.3	536.8	537.3	1596.3	537.3	1596.8	503.4	503.4	503.3
50	2682.5	836.4	836.2	2681.5	835.8	2680.0	895.0	895.7	895.3
65	4303.5	1300.6	1299.4	4298.1	1298.4	4294.8	1468.4	1468.5	1469.5
80	7612.4	2445.0	2445.7	7592.0	2441.5	7598.6	2542.1	2543.7	2543.9

Table 20: Non-zero components of the stiffness matrix C [MPa] of FK_{Solid} configuration as a function of the volume fraction.

	FK_{Solid}								
SV/TV [%]	C_{11}	C_{12}	C_{13}	C_{22}	C_{23}	C_{33}	C_{44}	C_{55}	C_{66}
10	61.6	28.1	28.1	61.5	28.0	61.5	12.3	12.3	12.3
25	548.3	209.1	209.5	545.9	208.4	547.3	154.5	155.1	154.9
35	1120.1	382.3	381.5	1118.9	381.6	1117.0	361.6	361.7	361.8
50	2185.7	682.3	681.7	2183.6	681.2	2181.9	761.2	761.1	761.3
65	3696.6	1122.1	1121.7	3686.2	1119.9	3688.1	1309.2	1310.5	1310.7
80	6037.3	1879.1	1878.9	6022.3	1875.4	6023.1	2104.2	2106.4	2106.2

Table 21: Non-zero components of the stiffness matrix C [MPa] of G_{Sheet} configuration as a function of the volume fraction.

	G_{Sheet}								
SV/TV [%]	C_{11}	C_{12}	C_{13}	C_{22}	C_{23}	C_{33}	C_{44}	C_{55}	C_{66}
10	215.4	84.4	84.4	215.6	84.4	215.4	67.2	67.1	67.2
25	794.9	312.6	312.7	794.7	312.9	795.4	279.8	279.3	279.5
35	1338.6	490.1	491.0	1336.7	490.5	1339.4	497.7	498.0	497.5
50	2382.1	808.4	808.8	2377.9	807.4	2377.2	910.6	911.2	910.9
65	3857.2	1253.7	1253.8	3856.5	1253.6	3857.6	1455.5	1456.0	1456.1
80	6631.3	2113.9	2114.5	6618.7	2111.5	6618.5	2287.0	2288.9	2288.8

Table 22: Non-zero components of the stiffness matrix C [MPa] of G_{Solid} configuration as a function of the volume fraction.

	G_{Solid}								
SV/TV [%]	C_{11}	C_{12}	C_{13}	C_{22}	C_{23}	C_{33}	C_{44}	C_{55}	C_{66}
10	28.9	5.6	5.6	28.8	5.6	28.9	2.6	2.6	2.6
25	485.1	141.2	141.3	482.7	140.9	484.4	137.5	138.3	138.4
35	1074.5	289.9	290.0	1068.9	288.9	1071.5	338.3	339.2	339.5
50	2175.1	570.6	570.0	2172.6	569.8	2171.3	725.8	726.9	727.0
65	3672.3	1003.9	1004.6	3664.6	1004.1	3672.4	1251.9	1252.5	1252.6
80	5802.5	1712.5	1713.6	5779.8	1708.6	5786.4	1973.0	1975.7	1976.0

Table 23: Non-zero components of the stiffness matrix C [MPa] of I-WP_{Sheet} configuration as a function of the volume fraction.

	I-WP_{Sheet}								
SV/TV [%]	C_{11}	C_{12}	C_{13}	C_{22}	C_{23}	C_{33}	C_{44}	C_{55}	C_{66}
10	239.4	75.2	75.5	239.6	75.5	239.6	88.1	88.0	88.0
25	895.3	259.1	259.1	895.3	259.1	895.3	271.3	271.2	271.1
35	1605.9	432.2	431.7	1604.9	432.4	1605.8	456.8	456.4	456.6
50	2906.0	757.8	758.0	2903.5	758.1	2903.4	836.9	836.9	837.0
65	4744.0	1294.8	1295.0	4736.8	1292.9	4735.4	1441.4	1442.5	1442.2
80	8343.9	2712.4	2716.7	8314.3	2710.0	8331.8	2775.7	2778.3	2776.5

Table 24: Non-zero components of the stiffness matrix C [MPa] of I-WP_{Solid} configuration as a function of the volume fraction.

	I-WP_{Solid}								
SV/TV [%]	C_{11}	C_{12}	C_{13}	C_{22}	C_{23}	C_{33}	C_{44}	C_{55}	C_{66}
10	115.0	98.8	98.8	115.0	98.8	114.9	98.9	98.9	98.9
25	554.5	351.0	350.9	555.3	351.3	554.9	367.1	366.9	366.9
35	1068.7	551.7	553.0	1067.5	551.9	1070.2	596.2	596.8	596.2
50	2257.5	894.9	896.0	2255.3	895.2	2255.5	1008.0	1008.3	1007.9
65	4202.6	1382.6	1381.0	4198.5	1380.6	4195.5	1570.3	1571.2	1571.9
80	7362.0	2348.4	2348.9	7352.4	2346.1	7354.5	2479.2	2480.6	2481.1